Voltage-Driven Magnetization Switching via Dirac Magnetic Anisotropy and Spin-Orbit Torque in Topological-Insulator-Based Magnetic Heterostructures

Takahiro Chiba[1,*] and Takashi Komine[2]

[1]*National Institute of Technology, Fukushima College, 30 Nagao, Kamiarakawa, Taira, Iwaki, Fukushima 970-8034, Japan*

[2]*Graduate School of Science and Engineering, Ibaraki University, 4-12-1 Nakanarusawa, Hitachi, Ibaraki 316-8511, Japan*

Electric field control of magnetization dynamics is fundamentally and technologically important for future spintronic devices. Here, based on electric field control of both magnetic anisotropy and spin-orbit torque, two distinct methods are presented for switching the magnetization in topological-insulator– (TI) magnetic-TI hybrid systems. The magnetic anisotropy energy in magnetic TIs is formulated analytically as a function of the Fermi level, and it is confirmed that the out-of-plane magnetization is always favored for the partially occupied surface band. Also proposed is a transistorlike device with the functionality of a nonvolatile magnetic memory that uses voltage-driven writing and the (quantum) anomalous Hall effect for readout. For magnetization reversal, by using parameters of Cr-doped $(Bi_{1-x}Sb_x)_2Te_3$, we find the estimated source-drain current density and gate voltage are on the order of 10^4–10^5 A/cm^2 and 0.1 V, respectively, below 20 K and the writing requires no external magnetic field. Also discussed is the possibility of magnetization switching by the proposed method in TI–ferromagnetic-insulator bilayers with the magnetic proximity effect.

I. INTRODUCTION

Electrical control of magnetism is essential for the next generation of spintronic technologies, such as non-volatile magnetic memory, high-speed logic, and low-power data transmission [1]. In these technologies or devices, the magnetization direction of a nanomagnet is controlled by an electrically driven torque rather than an external magnetic field. A representative torque is the current-induced spin-orbit torque (SOT) [2] in heavy-metal–ferromagnet heterostructures, wherein the spin Hall effect in the heavy metal [3,4] and/or the Rashba-Edelstein effect (also known as the inverse spin-galvanic effect) at the interface [5] play crucial roles in generating the torque. Recently, several experiments have reported a giant-SOT efficiency in topological-insulator- (TI) based magnetic heterostructures such as both TI–magnetic-TI [6] and TI–ferromagnetic-metal (FM) [7,8] hybrid systems. A TI has a metallic surface state in which the spin and momentum are strongly correlated (known as spin-momentum locking) because of a strong spin-orbit inter-action in the bulk state [9,10], which is expected to lead to the giant SOT [11]. Indeed, magnetization reversal by SOT has been proposed theoretically [12–15] and demonstrated

experimentally in magnetic TIs [6,16,17] as well as TI-ferromagnet bilayers [18–23]. Remarkably, the critical current density required for switching is on the order of 10^5 A/cm^2, which is much smaller than the corresponding values (10^6–10^8 A/cm^2) for heavy-metal–ferromagnet heterostructures [3–5]. In particular, the magnetization switching of magnetic TIs is more efficient: Yasuda *et al.* [17] succeeded in reducing the switching current density by means of a current pulse injected parallel to a bias magnetic field, whereas Fan *et al.* [16] realized magnetization reversal by means of a scanning gate voltage with a small constant current and in-plane magnetic field.

Another important method for controlling magnetic properties is the electric field effect in magnets, such as controlling ferromagnetism in dilute magnetic semiconductors [24], manipulating magnetic moments in multiferroic materials [25], and changing the magnetic anisotropy in an ultrathin film of ferromagnetic metal [26–28]. In particular, voltage control of magnetic anisotropy (VCMA) in ferromagnets promises energy-efficient reversal of magnetization by means of what is known as voltage torque, which has been demonstrated by use of a pulsed voltage under a constant-bias magnetic field in a magnetic tunnel junction [29]. This approach is based on the clocking scheme in which one first sets the ferromagnet to an initial stable state under the application of an external

*t.chiba@fukushima-nct.ac.jp

bias and then inputs the signal voltage pulse to determine the final state. Recent experiments using heavy-metal–ferromagnet–oxide heterostructures have demonstrated that the critical current for SOT-driven switching of perpendicular magnetization can be modulated by an electric field via VCMA [30,31]. By contrast, the electric field effect in a magnetic TI [32,33] and a TI–ferromagnetic-insulator (FI) bilayer [34,35] has been investigated to date in terms of the voltage-torque-driven magnetization dynamics. Semenov *et al.* [34] demonstrated magnetization rotation between the in-plane and out-of-plane directions by VCMA at the TI/FI interface. Therefore, it is highly desirable to control the magnetic anisotropy and SOT simultaneously by means of the electric field in TI-based magnetic heterostructures, which may lead to magnetization switching that is more energetically efficient.

In this paper, inspired by the SOT and VCMA approaches for magnetization control, we combine them and present two distinct clocking methods for magnetization switching in TI–magnetic-TI hybrid systems. First, we model the current-induced SOT and magnetic anisotropy energy (MAE) in TI-based magnetic heterostructures as a function of the Fermi level to determine a stable magnetization direction at the electrostatic equilibrium. Then we propose a transistorlike device with the functionality of a nonvolatile magnetic memory that uses (i) VCMA writing that requires no external magnetic field and (ii) readout based on the anomalous Hall effect. For the magnetization reversal, we estimate the source-drain current density and gate voltage. Finally, we show the switching phase diagram for the input pulse width and voltages as a guide to realizing the proposed method of magnetization reversal. We also discuss the possibility of using the proposed method for magnetization reversal in TI/FI bilayers with magnetic proximity [36–38] at the interface.

II. MODEL

We begin this section by deriving the current-induced SOT in TI-based magnetic heterostructures by using the current-spin correspondence of two-dimensional (2D) Dirac electrons on the TI surface. Next, in the same system we formulate the MAE analytically to determine a stable magnetization direction at the electrostatic equilibrium and to reveal the controllability of the VCMA effect. To model the SOT and VCMA, we consider 2D massless Dirac electrons on the TI surface, which is exchange coupled to the homogeneous localized moment of a magnetic TI (or an attached FI as discussed in Sec. IV B). When the surface electrons interact with the localized moment, they have an exchange interaction that can be modeled by a constant spin splitting Δ along the magnetization direction with unit vector $\mathbf{m} = \mathbf{M}/M_s$ (in which $\mathbf{M}$ is the magnetization vector with the saturation magnetization M_s) [39]. Then, the following 2D Dirac Hamiltonian provides a simple model

for the electronic structure of the TI surface state:

$$\mathcal{H}_{\mathbf{k}} = \hbar v_F \hat{\boldsymbol{\sigma}} \cdot \left(\mathbf{k} \times \hat{\mathbf{z}} \right) + \Delta \hat{\boldsymbol{\sigma}} \cdot \mathbf{m}, \qquad (1)$$

where $h = 2\pi\hbar$ is the Planck constant, v_F is the Fermi velocity of the Dirac electrons, $\hat{\boldsymbol{\sigma}}$ is the Pauli matrix operator for the spin, and Δ is the exchange interaction. For simplicity, we ignore here the particle-hole asymmetry in the surface bands. Introducing the polar angle θ and azimuthal angle φ for $\mathbf{m} = (\cos\varphi\sin\theta, \sin\varphi\sin\theta, \cos\theta)$, we can express the energy dispersion of the Hamiltonian (1) as

$$E_{\mathbf{k}s} = s\sqrt{(\hbar v_F k)^2 + \Delta^2 - 2\hbar v_F k \Delta \sin\theta \sin(\varphi - \varphi_k)}, \qquad (2)$$

where $s = \pm$ corresponds to the upper and lower bands, and $\cos\theta_{\mathbf{k}} = \Delta\cos\theta/|E_{\mathbf{k}s}|$ and $\tan\varphi_{\mathbf{k}} = k_y/k_x$ are the polar and azimuthal angles, respectively, of the spinors on the Bloch sphere.

A. Current-induced spin-orbit torque

We begin by discussing a current-induced SOT applied to the magnetization in TI-based magnetic heterostructures [12,14,15,40–43]. The SOT stems from the exchange interaction between the magnetization and the electrically induced nonequilibrium spin polarization $\boldsymbol{\mu}$ (in the unit of reciprocal square meters) [7,11], which can be described by

$$\mathbf{T}_{\mathrm{SO}} = -\gamma \frac{\Delta\boldsymbol{\mu}}{M_s d} \times \mathbf{m}, \qquad (3)$$

where γ is the gyromagnetic ratio and d is the thickness of the ferromagnetic layer (magnetic TI). In short, the SOT is obtained by calculating the electrically induced spin polarization on the TI surface.

As a characteristic feature of the Dirac Hamiltonian (1), the spin operator $\hat{\boldsymbol{\sigma}}$ is directly proportional to the velocity operator $\hat{\mathbf{v}} = \partial\mathcal{H}_{\mathbf{k}}/(\hbar\partial\mathbf{k}) = v_F\hat{\mathbf{z}} \times \hat{\boldsymbol{\sigma}}$ due to the spin-momentum lock. In this sense, we can identify the nonequilibrium spin polarization $\boldsymbol{\mu}$ with the electric current $\mathbf{J}$ on the TI surface; namely,

$$\boldsymbol{\mu} = -\frac{1}{ev_F}\hat{\mathbf{z}} \times \mathbf{J}, \qquad (4)$$

where $-e$ ($e > 0$) is the electron charge. In the following, we use $\boldsymbol{\mu}$ and $\mathbf{J}$ to denote the quantum statistical expectation values of $\hat{\boldsymbol{\sigma}}$ and $\hat{\mathbf{j}} = -e\hat{\mathbf{v}}$, respectively. We emphasize that the nonequilibrium spin polarization involves only in-plane spin components. Hence, the in-plane component of the spin susceptibility corresponds to the electric conductivity via Eq. (4). In the framework of Boltzmann transport theory and the Kubo formula, previous studies

[41,42,44–47] calculated the longitudinal and transverse (anomalous Hall) conductivities on magnetized TI surfaces by assuming a short-range impurity potential with Gaussian correlations $\langle \hat{V}(r_1)\hat{V}(r_2)\rangle_{\text{imp}} = nV_0^2\delta(r_1 - r_2)$, in which n is the impurity concentration, V_0 is the scattering potential, and $\langle\cdots\rangle_{\text{imp}}$ indicates an ensemble average over randomly distributed impurities. For an electric field $\mathbf{E}$ along the TI surface, the driving sheet current can be written as $\mathbf{J} = \sigma_L\mathbf{E} + \sigma_{\text{AH}}\hat{\mathbf{z}} \times \mathbf{E}$, with [42]

$$\sigma_L = \frac{e^2}{2h}\frac{E_F\tau}{\hbar}\frac{1 - \xi^2 m_z^2}{1 + 3\xi^2 m_z^2},$$

$$\sigma_{\text{AH}} = -\frac{4e^2}{h}\xi m_z\frac{1 + \xi^2 m_z^2}{\left(1 + 3\xi^2 m_z^2\right)^2}, \tag{5}$$

where $\tau = 4\hbar\left(\hbar v_F\right)^2/nV_0^2 E_F$ is the transport relaxation time of massless Dirac electrons within the Born approximation, $\xi = \Delta/E_F$ with the Fermi level E_F measured from the original band-teaching (Dirac) point, and m_z denotes the z component of $\mathbf{m}$. In Eq. (5), σ_{AH} is independent of the impurity parameters but diagrammatically contains the side-jump and skew-scattering contributions as well as the intrinsic contribution associated with the Berry curvature of the surface bands [44,46]. According to Eq. (4), the current-induced spin polarization for $\mathbf{E} = E_x\hat{\mathbf{x}}$ is therefore

$$\boldsymbol{\mu} = -\frac{1}{ev_F}\left(-\sigma_{\text{AH}}\mathbf{E} + \sigma_L\hat{\mathbf{z}} \times \mathbf{E}\right) \equiv \mu_x m_z\hat{\mathbf{x}} + \mu_y\hat{\mathbf{y}}, \tag{6}$$

where

$$\mu_x = -\frac{4eE_x}{hv_F}\Delta\frac{E_F\left(E_F^2 + \Delta^2 m_z^2\right)}{\left(E_F^2 + 3\Delta^2 m_z^2\right)^2}, \tag{7}$$

$$\mu_y = -\frac{eE_x}{2hv_F}\frac{E_F\tau}{\hbar}\frac{E_F^2 - \Delta^2 m_z^2}{E_F^2 + 3\Delta^2 m_z^2}. \tag{8}$$

Equations (7) and (8) are substantially equivalent to the current-induced nonequilibrium spin density that Ndiaye et al. [15] calculated directly by using the Kubo-Streda formula involving the spin-vertex correction. Note that μ_x originates from the magnetoelectric coupling (the so-called Chern-Simons term) [12,39] that is proportional to the anomalous Hall conductivity [see Eq. (6)]. Furthermore, μ_y stems from the Rashba-Edelstein effect due to the spin-momentum locking on the TI surface [40].

From Eqs. (3) and (6), we finally obtain the form of SOT arising from the TI surface [15,42] (see Appendix A for the current expression for SOT); namely,

$$\mathbf{T}_{\text{SO}} = \gamma\frac{\Delta\mu_x}{M_s d}m_z\mathbf{m} \times \hat{\mathbf{x}} + \gamma\frac{\Delta\mu_y}{M_s d}\mathbf{m} \times \hat{\mathbf{y}}. \tag{9}$$

The first term acts as a dampinglike (DL) torque but one

that is quite different from that of the spin Hall effect in traditional heavy-metal–ferromagnet heterostructures [3,4]. For the in-plane-magnetization configuration ($m_z = 0$), this DL torque vanishes because of the absence of the magnetoelectric coupling via the anomalous Hall effect, whereas the SOT driven by the spin Hall effect acts on the magnetization. Meanwhile, despite its origin, the second term acts as only a fieldlike (FL) torque. This feature is also different from that of the Rashba-Edelstein effect in the usual 2D ferromagnetic Rashba systems in which there might be both FL and DL contributions [48,49]. Figures 1(a) and 1(b) show the E_F dependence of the x and y components, respectively, of $\Delta\boldsymbol{\mu}$ (in the unit of joules per square meter) for different values of the surface band gap. For this calculation, Δ is used within the values reported experimentally in magnetically doped [50] and FI-attached [37,51] TIs. We also use $n = 10^{12}$ cm^{-2} and $V_0 = 0.2$ keV Å^2 as impurity parameters on the basis of an analysis of the transport properties of a TI surface [52]. These impurity parameters can reproduce the experimentally observed longitudinal resistance (approximately 10 kΩ) in magnetic TIs. Remarkably, as seen in Fig. 1(a), even when the Fermi level is inside the surface band gap
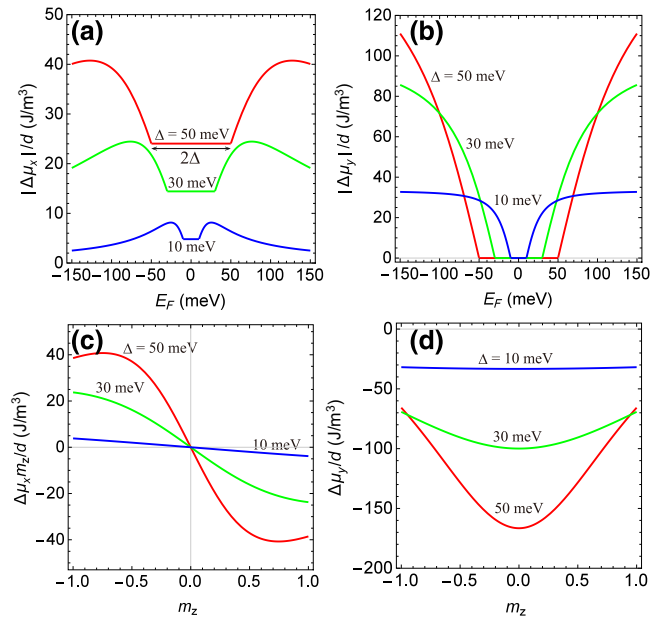

FIG. 1. Current-induced nonequilibrium spin polarization $\Delta\boldsymbol{\mu}/d$ scaled by thickness d of a ferromagnet as a function of E_F for different values of Δ (with $m_z = 1$): (a) x component $\Delta\mu_x/d$; (b) y component $\Delta\mu_y/d$; (c) $\Delta\mu_x/d$ and (d) $\Delta\mu_y/d$ at $E_F = 95$ meV (corresponding carrier density approximately 10^{12} cm^{-2}) as a function of m_z for different values of Δ. In these graphs, we use $v_F = 4.0 \times 10^5$ m/s, $d = 10$ nm, and $E_x = 0.1$ V/μm. The details of the calculations are given in the text.

$(E_F < |\Delta|)$, the x component survives as [12,41]

$$\mu_x = -\frac{eE_x}{2hv_F} = -\frac{1}{ev_F}\sigma_{\text{QAH}}E_x, \qquad (10)$$

where $\sigma_{\text{QAH}} = e^2/(2h)\,\text{sgn}\,m_z$ characterizes the quantum anomalous Hall effect on the magnetized TI surface [53], reflecting the topological nature of 2D massive Dirac electrons. By contrast, because of the Rashba-Edelstein effect, the y component shown in Fig. 1(b) survives in only the metallic surface states $(E_F \geq |\Delta|)$. Figures 1(c) and 1(d) show the m_z dependence of the x and y components, respectively, of $\Delta\boldsymbol{\mu}$ for different values of the surface band gap. In these plots, we include m_z in the x component of $\Delta\boldsymbol{\mu}$. Reflecting the anomalous Hall effect on the magnetized TI surface, the x component is odd on magnetization reversal, whereas the y component is even on magnetization reversal because it is proportional to σ_L via the Rashba-Edelstein effect.

B. Dirac magnetic anisotropy

Here, to evaluate the VCMA effect in TI-based magnetic heterostructures, we investigate the MAE associated with the exchange interaction in Eq. (1). The MAE is defined as the difference in the sums over occupied states of energy dispersions (2) with $\theta = 0$ as the reference state [54]; namely,

$$U_{\text{MAE}} = \sum_{\mathbf{k}s}^{\text{occ}} E_{\mathbf{k}s}(\theta) - \sum_{\mathbf{k}s}^{\text{occ}} E_{\mathbf{k}s}(\theta = 0). \qquad (11)$$

Expanding Eq. (11) around $\theta \approx 0$ leads to $U_{\text{MAE}} \approx K_u \sin^2\theta$, where the uniaxial magnetic anisotropy constant K_u (in the unit of joules per square meter) is given by

$$K_u = -\sum_{\mathbf{k}s}^{\text{occ}} s\frac{(\hbar v_F k)^2 \Delta^2 \sin^2(\varphi - \varphi_{\mathbf{k}})}{2\left[(\hbar v_F k)^2 + \Delta^2\right]^{3/2}}. \qquad (12)$$

The sign of K_u specifies the type of MAE; namely, perpendicular magnetic anisotropy (PMA; $K_u > 0$) or easy-plane magnetic anisotropy ($K_u < 0$). For the partially occupied energy bands, we have $K_u > 0$; that is, PMA is always favored by the magnetization coupled with Dirac electrons on the TI surface. A qualitative understanding of the characteristic PMA is given by a gain of electronic free energy associated with the exchange interaction between the Dirac electrons and the localized moment. When the magnetization is along the out-of-plane direction, a surface band gap ($2\Delta m_z$) emerges in the massless Dirac dispersion, which reduces the electron group velocity (kinetic energy). Meanwhile, for the in-plane magnetization orientation, the exchange interaction merely shifts the surface band in the k space. In terms of the exchange interaction

maximizing the energy gain of the Dirac electron system, the case possessing the surface band gap is expected to be more favorable with lower electronic free energy than that with the surface bands shifted by an in-plane magnetization, whose scenario can be interpreted as being analogous to the Peierls transition in electron-lattice coupled systems [50].

To integrate Eq. (12), we assume hereinafter that the low-energy Dirac Hamiltonian (1) is a valid description for $k \leq k_c$ with a momentum cut $k_c = \sqrt{\Delta_c^2 - \Delta^2}/\hbar v_F$ [55] in which $2\Delta_c$ is the bulk band gap of TIs induced by the band inversion due to the spin-orbit interaction. We also define the Fermi wave vector $k_F = \sqrt{E_F^2 - \Delta^2}/\hbar v_F$, as shown in Fig. 2(a). Without loss of generality, we assume the case in which E_F crosses the upper surface band; namely, $E_F > \Delta$. Then, we obtain the magnetic anisotropy constant by integration over the relevant energy range as

$$K_u = \frac{\Delta^2}{8\pi(\hbar v_F)^2}\left[\Delta_c - E_F - \left(\frac{1}{E_F} - \frac{1}{\Delta_c}\right)\Delta^2\right]. \qquad (13)$$

Up to the lowest order of Δ, Eq. (13) takes the simplest analytic from of $K_u = \Delta^2 k_c/8\pi\hbar v_F$, which corresponds to the out-of-plane MAE for $E_F \leq |\Delta|$ derived by Tserkovnyak *et al.* [55]. Figure 2(b) shows the E_F dependence of K_u for different values of the bulk and surface band gaps. In this plot, $\Delta_c = 150$ meV and $\Delta_c = 100$ meV correspond to the bulk band gaps for $\text{Bi}_{2-x}\text{Sb}_x\text{Te}_{3-y}\text{Se}_y$ (BSTS) and $(\text{Bi}_{1-x}\text{Sb}_x)_2\text{Te}_3$ (BST) [10], respectively. Because we assume that the surface states have energy dispersions with particle-hole symmetry, the magnetic anisotropy constant retains the form of Eq. (13) in the case
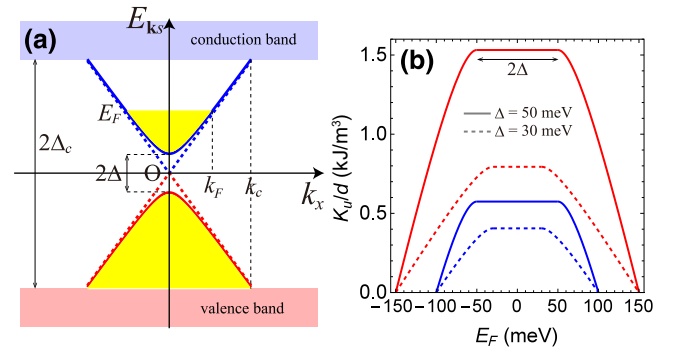

FIG. 2. (a) Massless (dashed line) and massive (solid line) surface state dispersions at $k_y = 0$ in which E_F denotes the Fermi level measured from the Dirac point ($E_{\mathbf{k}s} = 0$) of the original massless surface bands, 2Δ is the surface band gap due to an exchange interaction, and $2\Delta_c$ is the bulk band gap. k_F and k_c correspond to the Fermi wave vector and the cutoff wave vector, respectively. (b) Scaled magnetic anisotropy energy K_u/d as a function of E_F for different values of Δ_c and Δ. Red and blue lines are for $\Delta_c = 150$ meV and $\Delta_c = 100$ meV, respectively. In this plot, we use $v_F = 4.0 \times 10^5$ m/s and $d = 10$ nm.

in which E_F crosses the lower surface band; namely, $E_F < -\Delta$. Hence, K_u is maximum with the form of $K_u|_{E_F=|\Delta|}$ for $E_F \le |\Delta|$ and decreases apart from the energy level of $\pm\Delta$. The reason is that there are simply fewer active electrons for $E_F < -\Delta$, while for $E_F > \Delta$ the energy decrease in the lower band is compensated partially by the upper-band energy increase in conductive electrons.

At the end of this section, we compare the formulated MAE with a recent experiment using Cr-doped BST thin films that are sandwiched by two different dielectrics and hence have the Dirac electron systems on each interface [16]. The magnetic anisotropy field due to Eq. (13) is defined by $B_K = 2K_u/M_s d$. For the Cr-doped BST films with $d \approx 7$ nm, a calculated result is $B_K = 117$ mT ($K_u/d = 0.5$ kJ/m^3), while an experiment reports $B_K \approx 570$ mT without an electric gate [16]. In this calculation, we choose the following parameters for Cr-doped BST: $\Delta_c = 100$ meV, $\Delta = 30$ meV, $v_F = 4.0 \times 10^5$ m/s, $M_s = 8.5 \times 10^3$ A/m, and an electron (hole) carrier density of 1.0×10^{12} cm^{-2} (0.2×10^{12} cm^{-2}) [corresponding to $|E_F| = 98$ meV ($|E_F| = 51$ meV)] for each interface [16]. The difference in B_K might come from our disregarding the realistic particle-hole asymmetry induced by the higher-order k term of the energy dispersion, which makes a sharper electronic density of states in the surface valence band and enhances the hole-mediated Dirac PMA up to $K_u/d = 8$ kJ/m^3 [34]. In this respect, our simple Dirac model cannot reflect the detail of the realistic surface band but can capture the permissible magnitude of B_K. Therefore, the above comparison implies that the interfacial Dirac PMA gives a significant contribution to the magnetic anisotropy in dilute magnetic TIs.

III. MAGNETIZATION SWITCHING

To demonstrate magnetization switching via SOT and VCMA, we propose a field-effect-transistor- (FET) like device with a magnetic TI film as a conduction-channel layer [16] in which source-drain (V_S) and gate (V_G) voltages are applied, as shown in Fig. 3. To investigate the macroscopic dynamics of the magnetization in the device, we solve the Landau-Lifshitz-Gilbert equation including the SOT (9); namely,

$$\frac{d\mathbf{m}}{dt} = -\gamma \mathbf{m} \times \mathbf{B}_{\text{eff}} + \alpha_{\text{eff}}\mathbf{m} \times \frac{d\mathbf{m}}{dt} + \mathbf{T}_{\text{SO}}(V_G), \quad (14)$$

where $\mathbf{B}_{\text{eff}}$ is an effective magnetic field obtained by finite $\mathbf{m}$ functional derivatives of the total energy U_M, namely, $\mathbf{B}_{\text{eff}} = -\delta U_M/M_s \delta\mathbf{m}$, and α_{eff} denotes the effective Gilbert damping constant. As discussed in Sec. II B, the interfacial Dirac PMA gives a significant contribution to the magnetic anisotropy in dilute magnetic TIs. Because of the thin magnetic TI in Fig. 3, we assume that U_M consists of the MAE (13) and the magnetostatic energy that generates a
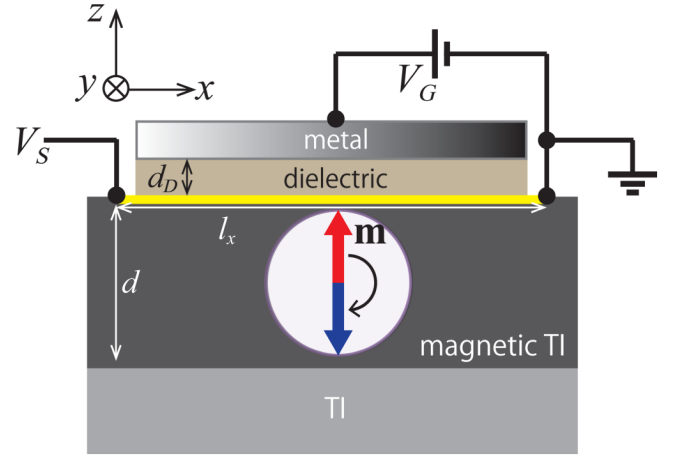

FIG. 3. Geometry (side view) of the FET-like device comprising a magnetic-TI film (with thickness d) sandwiched between a nonmagnetic TI and a dielectric attached to a top electric gate V_G in which the Dirac electron system should appear on the top surface of the magnetic TI [17]. d_D is the thickness of the dielectric and l_x is the length of the conduction channel. V_S is the voltage difference between the source electrode and the drain electrode. Current flows on the x-y plane depicted by a yellow line that corresponds to the TI surface state. The arrows denote the initial (red) and final (blue) magnetization directions in the magnetization reversal.

demagnetization field; that is,

$$U_M = \frac{1}{d}K_u(V_G)\left(1 - m_z^2\right) + \frac{1}{2}\mu_0 M_s^2 m_z^2, \quad (15)$$

where μ_0 is the permeability of free space. As discussed in Sec. II, both MAE and SOT depend on the position of E_F, which can be controlled electrically via (see Appendix B for details)

$$E_F(V_G) = \hbar v_F \sqrt{4\pi\left(n_{\text{int}} + \frac{\Delta^2}{4\pi\,(\hbar v_F)^2} + \frac{\epsilon}{ed_D}V_G\right)}, \quad (16)$$

where ϵ is the permittivity of a dielectric of thickness d_D and n_{int} is the intrinsic carrier density at $V_G = 0$. In this study, for the dielectric layer with $d_D = 20$ nm, we adopt a typical insulator, namely, Al$_2$O$_3$ (for which the relative permittivity $\epsilon/\epsilon_0 = 9.7$) [16,56].

Because the ferromagnetic Curie temperature of Cr-doped BST is less than 35 K [57], we first consider magnetization switching at zero temperature. The influence of finite temperatures on the magnetization switching is discussed in Sec. IV C. The equilibrium magnetization direction with neither V_S nor V_G is determined by minimizing Eq. (15) regarding the polar angle θ. However, for simplicity, we assume that $\theta \approx 0°$ at the electrostatic equilibrium. This assumption is permissible because hereinafter we consider a magnetic TI such as Cr-doped BST

with a very small M_s (8.5×10^3 A/m [16]), ignoring the demagnetizing field effect from the second term in Eq. (15) at $V_G = 0$. For numerical simulation, Eq. (14) is solved by our setting $\theta = 1°$ and $\varphi = 0°$ as the initial conditions for $\mathbf{m}(t = 0)$. In the simulation, we choose the parameters for Cr-doped BST as $\Delta_c = 100$ meV, $\Delta = 30$ meV, $v_F = 4.0 \times 10^5$ m/s, $d = 7$ nm, $n = 10^{12}$ cm^{-2}, $V_0 = 0.2$ keV Å^2 [52], $n_{\text{int}} \approx 0$ cm^{-2} [corresponding to $E_F(V_G = 0) = \Delta = 30$ meV] [56,57], $\gamma = 1.76 \times 10^{11}$ T^{-1} s^{-1}, and $\alpha_{\text{eff}} = 0.1$. A large enhanced damping from 0.03 to 0.12 due to the strong spin-orbit interaction of TIs has been reported in TI–ferromagnetic-metal bilayers [58]. In addition, no modulation of α_{eff} is assumed during the duration of application of the gate voltage because we consider a thicker magnetic TI film ($d = 7$ nm) than the ferromagnetic metal used in the magnetic tunnel junction [59].

A. Switching via a source-drain current pulse J_S

We investigate the magnetization switching via a source-drain current pulse [17]. Under a static gate voltage [16], we apply a steplike voltage pulse of width t_S to the source electrode, as shown in Fig. 4(a) (see the upper panel). The applied gate voltage can reduce the energy barrier for the magnetization reversal due to the VCMA effect in Eq. (13). The resulting time evolution of $\mathbf{m}(t)$ is shown in Fig. 4(a) with the constant gate voltage turned on at $t = 0$. The lower panel shows clearly that m_z changes its sign by the pulsed-source-voltage inputs, demonstrating the out-of-plane magnetization switching. Furthermore, application of subsequent pulses switches the magnetization direction faithfully, and the change is independent of the pulse's sign. The estimated switching time between point 1 and point 2 (point 3 and point 4) is approximately

18 ns. In this simulation with static $V_G = 0.32$ V and $V_S = 1.5$ V, the magnetic anisotropy field B_K, the effective fields due to the DL SOT $B_{\text{DL}} = \Delta\mu_{x(y)}/M_s d$, and the FL SOT $B_{\text{FL}} = \Delta\mu_{x(y)}/M_s d$ are evaluated for $m_z = 1$ as $B_K = 21$ mT, $B_{\text{DL}} = 6.0$ mT, and $B_{\text{FL}} = 17$ mT, respectively. The calculated magnetic anisotropy field is 136 mT at $V_G = 0$. The estimated current density J_S [corresponding to B_{DL} (B_{FL})] is 1.9×10^5 A/cm^2 (see Sec. IV A for details), which is consistent with current densities of TI-based magnetic heterostructures [6,17–20,22]. Figures 4(b) and 4(c) show the magnetization-switching trajectories during the durations shown by numbers (1–4) in the upper panel in Fig. 4(a). An equilibrium magnetization almost along $\pm\hat{\mathbf{z}}$ is rotated steeply around the current-induced spin polarization ($\boldsymbol{\mu}$) by the pulsed SOT until the black star, after which B_K gradually stabilizes the magnetization with oscillations around the easy axis.

B. Switching via a pulsed gate voltage V_G

We also investigate the magnetization switching via a pulsed gate voltage. Under a constant source-drain bias, we apply a steplike voltage pulse of width t_G to the gate electrode, as shown in Fig. 5(a) (see the upper panel). The source-drain bias induces the spin polarization that takes the role of a constant-bias magnetic field [29], while the pulsed gate voltage reduces the energy barrier for the magnetization reversal via the VCMA effect during its duration. The resulting time evolution is shown in Fig. 5(a) with the source-drain bias turned on at $t = 0$. Figures 5(b) and 5(c) show the corresponding magnetization-switching trajectories in which an equilibrium magnetization at an initial state (1 or 3) is rotated steeply around the bias effective magnetic field (proportional to $\boldsymbol{\mu}$) by the SOT until the
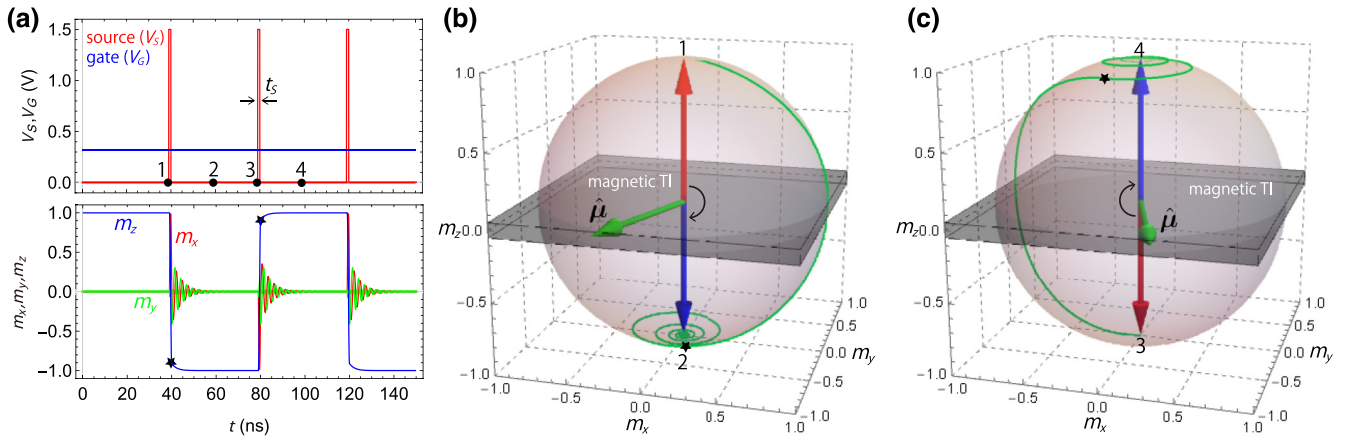

FIG. 4. (a) Time evolution of each component of magnetization with a pulsed source voltage (V_S). The numerical calculation is performed with static $V_G = 0.32$ V, $V_S = 1.5$ V, and $t_S = 1$ ns. (b),(c) Corresponding magnetization-switching trajectories during the duration (b) from 1 to 2 and (c) from 3 to 4 in the upper panel in (a). The vertical arrows denote the initial (red) and final (blue) magnetization directions in the magnetization reversal. The green arrow on the surface of the magnetic TI (black cube) indicates the direction of the current-induced spin polarization: $\hat{\boldsymbol{\mu}} = \boldsymbol{\mu}/|\boldsymbol{\mu}|$. The SOT is active from 1 (3) to the black star.
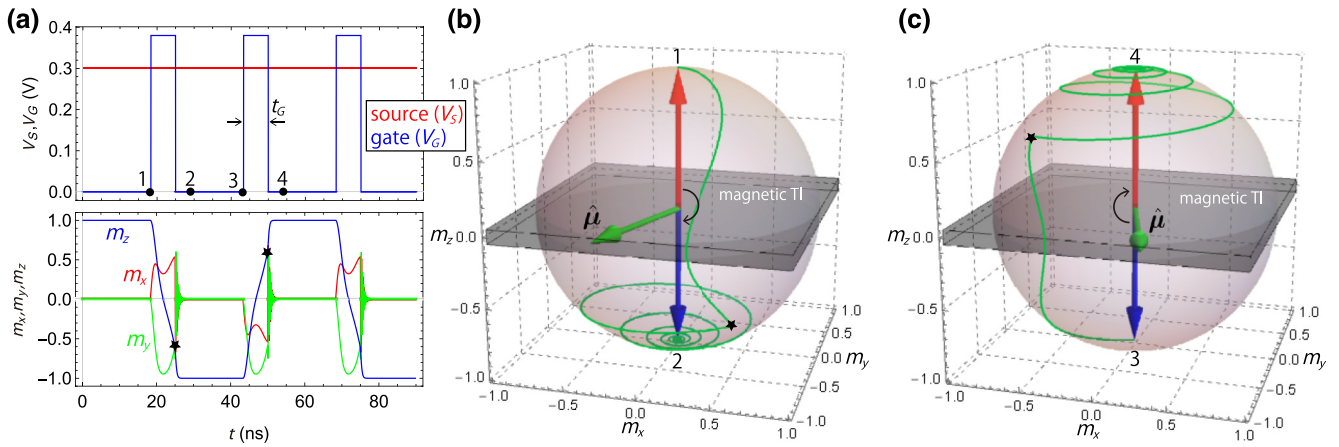
FIG. 5. (a) Time evolution of each component of magnetization with a pulsed gate voltage V_G. The numerical calculation is performed with $V_G = 0.38$ V, $V_S = 0.3$ V, and $t_G = 6.7$ ns. (b),(c) Corresponding magnetization-switching trajectories during the duration (b) from 1 to 2 and (c) from 2 to 3 in the upper panel in (a). The red, blue, and green arrows and the black star have the same meanings as in Fig. 4.

black star, after which B_K (= 136 mT at $V_G = 0$) aligns the magnetization direction with the easy axis by Gilbert damping. As shown, the z component of the magnetization changes sign by the pulsed-gate-voltage inputs, demonstrating the out-of-plane magnetization switching. The estimated switching time from the initial state to the final state is almost the same as the pulse width $t_G \sim 6.7$ ns. In this simulation with static $V_G = 0.38$ V and $V_S = 0.3$ V, we evaluate $B_K = 3.0$ mT, $B_{DL} = 1.2$ mT, and $B_{FL} = 3.6$ mT for $m_z = 1$. We emphasize that the current density J_S corresponding to the SOT is 4.1×10^4 A/cm², which is smaller than that of the pulsed-SOT method discussed above and the current densities of TI-based magnetic heterostructures reported to date [22].

C. Switching phase diagram

We conclude this study with a guide for realizing the proposed magnetization-switching methods. In particular, experimenters may be interested in how the final-state solution of m_z depends on the input pulse width and voltages. In Fig. 6, we use the parameters for Cr-doped BST. Figure 6(a) shows the phase diagram of m_z for a source-drain current pulse as a function of both t_S and V_G. The diagram is calculated up to $V_G \approx 0.39$ V, at which the Fermi level reaches the bottom of a bulk conduction band. The final-state solution of m_z oscillates rapidly depending on t_S rather than V_G, whereas the diagram has a threshold V_G in the vicinity of 0.32 V, at which the SOT competes with the anisotropy field. In Fig. 6 (b), we show the phase diagram of m_z for a pulsed gate voltage as a function of both t_G and V_S. Clearly, the final-state solution of m_z oscillates depending on both t_G and V_S, whereas switching tends to succeed in the short-pulse region of subnanosecond order. Consequently, switching will be achieved in the

wide pulse duration between the nanosecond and submicrosecond scales. In practice, the proposed device would be mounted by combination with semiconductor devices such as CMOS devices, whereas the switching speed of very-large-scale integration is not so fast at present. Hence,
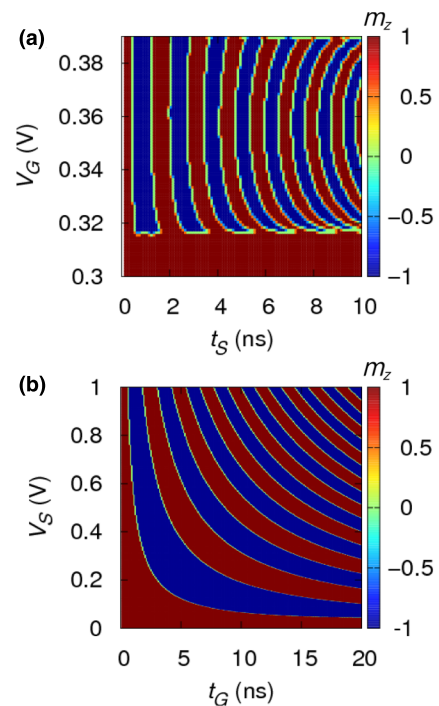

FIG. 6. (a) Final-state diagram of m_z at $V_S = 1.5$ V as a function of pulse duration t_S and gate voltage V_G. (b) Final-state diagram of m_z at $V_G = 0.39$ V as a function of pulse duration t_G and source-drain voltage V_S.

control with a pulse width of a few nanoseconds is considered realistic. Figure 6(b) shows that the controllability of the t_G pulse is better than that of the t_S pulse because of the width of the pulse. From the viewpoint of speed, it can be expected that the t_G pulse has better compatibility with very-large-scale integration.

IV. DISCUSSION

A. Source-drain current and Hall voltage: FET and memory operations

To evaluate the magnitude of current density (J_S) realizing the magnetization switching in Sec. III, we calculate the source-drain current flowing on the TI surface in Fig. 7(a). We also calculate the magnitude of the output Hall voltage (V_H) to read out a direction of the out-of-plane magnetization by its sign [60]. According to Eq. (5) and $E_x = V_S/l_x$, the corresponding quantities can be written as

$$J_S = \frac{\sigma_L(V_G)}{d}\frac{V_S}{l_x},$$ (17)

$$V_H = \frac{\sigma_{AH}(V_G)}{d}\frac{V_S}{l_x}l_y,$$ (18)

which are plotted in Figs. 7(b) and 7(c), respectively. In these plots, we use the same parameters as for Cr-doped BST in Sec. III. As a reminder, note again that $n_{int} \approx 0$ cm^{-2} [corresponding to $E_F(V_G = 0) = \Delta = 30$ meV] is assumed for the electrostatic equilibrium. Figure 7(d) shows the FET operation (on-off) of the proposed device. Clearly, we can switch the source-drain current by a reasonable gate voltage compared with modern FET devices. Therefore, combining this FET operation with the proposed magnetization-switching method promises a FET with the functionality of a nonvolatile magnetic memory [61]. The bit stored in this device is read out by measuring V_H and determining its sign. So, if $E_F(V_G = 0)$ is tuned within the surface band gap by the element substitution [56], the quantum anomalous Hall effect might allow the readout process to be free from energy dissipation due to Joule heating.

B. TI/FI bilayers

We discuss the possibility of magnetization switching in TI/FI bilayers with the magnetic proximity effect at the interface [36–38]. A device corresponding to Fig. 3 is proposed by our replacing the dielectric with a FI and the TI–magnetic-TI bilayer with a TI. In this case, it is easily shown that an exchange interaction between interface Dirac electrons and localized moments of the FI appears in the same form as that of the Dirac PMA given by Eq. (13) [34,55]. Then, the magnetization dynamics can be analyzed by use of the Landau-Lifshitz-Gilbert equation (14)
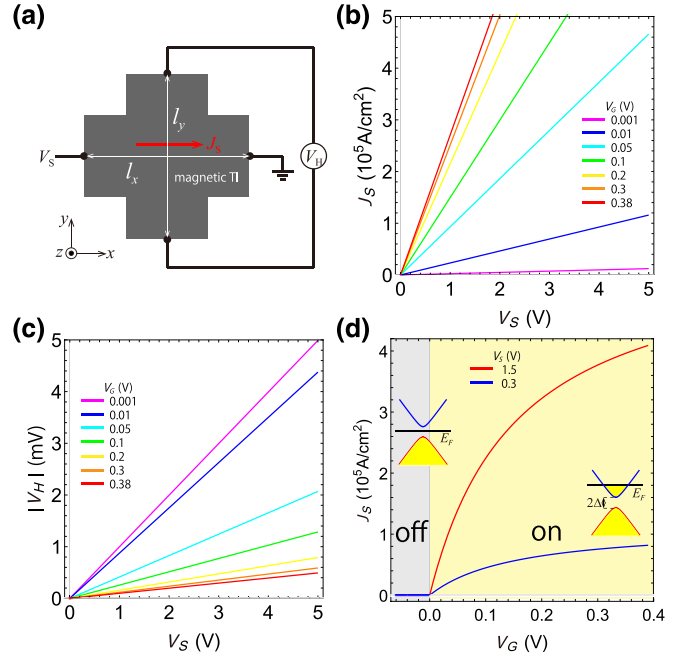

FIG. 7. (a) Top view of device proposed in Fig. 3 (here the gate and dielectric layers are hidden), where l_x and l_y are the lengths of the source-drain and Hall directions, respectively. (b) Source-drain current density J_S of proposed device versus V_S for different values of V_G. (c) Corresponding Hall voltage $|V_H|$ versus V_S for different values of V_G. (d) Transfer characteristics obtained for different values of V_S, indicating the FET operation (on-off) of the proposed device. The insets show the band pictures corresponding to the on-off states. In these plots, we assume $|m_z| = 1$, $d = 7$ nm, and $l_x = l_y = 10$ μm.

involving crystalline magnetic anisotropies (K_{CMA}) of the FI. Switching methods similar to those discussed in Sec. III will be achieved for a magnetically almost-isotropic FI with small net magnetization (desirably $K_{CMA}d/K_u \ll 1$ and $M_s \lesssim 10^5$ A/m), reducing the demagnetizing field effect. The potential candidates for the FI layer are 2D van der Waals ferromagnetic semiconductors [51,62] and rare-earth iron garnets [63–65] near their compensation point, where the intrinsic magnetic anisotropy and magnetostatic field become inferior to those of the Dirac PMA. However, the compensation points of the candidates are at a finite temperature; therefore, the thermal excitation of the TI bulk state and the effective magnetic field due to the thermal fluctuation of localized moments might affect the switching probability, which is beyond the scope of the present investigation. An alternative might be to use an insulating antiferromagnet with the A-type layered structure [66] that has no magnetostatic field because of the tiny net magnetization. A recent experiment reported that the TI surface states on Bi$_2$Se$_3$ produce a PMA in the attached soft ferrimagnet Y$_3$Fe$_5$O$_{12}$ [67].

So far, we have focused only on all-insulating systems (i.e., TI and FI), whereas TI/FM bilayer systems are

important for spintronic applications and experiments. It is necessary to consider the direct application of our model to the TI/FM bilayer represented by a pair of Bi_2Se_3 and permalloy (Py) for the following two reasons. First, our 2D model cannot capture the three-dimensional (3D) nature of the transport in the TI/FM bilayer. Indeed, in Bi_2Se_3/Py bilayers, most of the electric current shunts through the Py layer and conductive bulk states of the Bi_2Se_3 layer, which reduces the portion of the current interacting with the TI interface state. From this viewpoint, Fischer *et al.* [68] show that in the FM layer spin-diffusion transport perpendicular to the interface plays a crucial role in generating the DL torque. In contrast, on the basis of a 3D tight-binding model of the TI/FM bilayer, Ghosh *et al.* [43] demonstrate that a large DL SOT is generated by the Berry curvature of the TI interface state rather than the spin Hall effect of the bulk states. Second, orbital hybridization between the 3d transition metal and the TI deforms the TI surface states, which shifts the Dirac point to lower energy and generates Rashba-like metallic bands across the Fermi level [69,70]. Besides, the hexagonal-warping effect might be important for Bi_2Se_3 with a relatively large E_F due to its crystal symmetry. According to Li *et al.* [71], the Berry curvature for hexagonal-warping bands involves not only components of the out-of-plane magnetization but also those of the in-plane magnetization, which implies that the in-plane magnetization can contribute to the DL SOT. The hexagonal-warping term is important under threefold-rotational symmetry as in the Bi_2Se_3 crystal structure, while it becomes small in bulk insulating TIs (our focus) such as BSTS and Cr-doped BST due to reduction of the symmetry by the elemental substitution [72].

C. Influence of finite temperatures

For the experimental probe of our proposal, one may be interested in how finite temperatures affect the magnetization switching. In our model, there are mainly three temperature effects: (i) temperature dependence of physical quantities of TIs (σ_L, σ_{AH}, and K_u), (ii) the thermal excitation of the TI bulk states at finite temperatures, and (iii) a random magnetic field due to the thermal fluctuation of localized moments, potentially leading to a switching error. Cases (i) and (ii) are due to electronic properties, while case (iii) is in usual treated by magnetization dynamics.

For case (i), at low temperatures that satisfy $k_B T \ll \Delta < E_F$ (k_B is the Boltzmann constant), we can regard the Fermi-Dirac distribution function $f(E) \approx \Theta(E - E_F)$ as the step function and then ignore the temperature dependence of σ_L, σ_{AH}, and K_u. Indeed, when we set $\Delta = 30$ meV and 30 meV $\leq E_F \leq 100$ meV for the system, the above condition is satisfied below 30 K ($k_B T \approx 2.6$ meV); that is, a temperature less than the Curie temperature of magnetic TIs or FIs discussed in Sec. IV B.
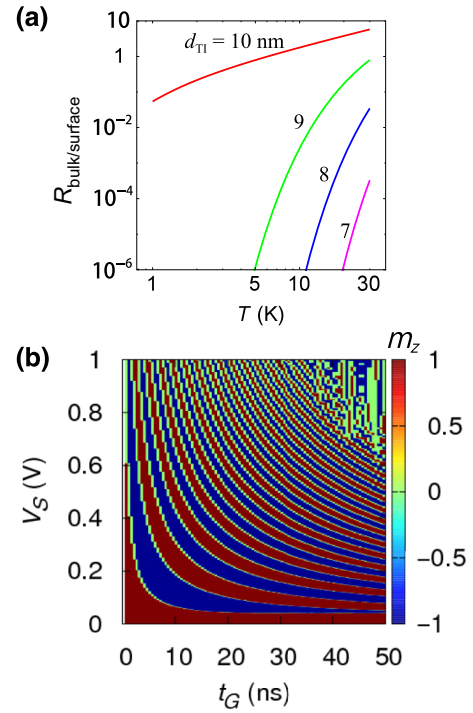

FIG. 8. (a) $R_{\text{bulk/surface}} = n_b d_{\text{TI}}/n_s$ as a function of T for different magnetic-TI thicknesses d_{TI}. (b) Final-state diagram at $T = 20$ K as a function of pulse duration t_G with $V_G = 0.39$ V and source-drain voltage V_S. The influence of the thermal fluctuation emerges in a longer t_G region with larger V_S.

For case (ii), based on the model in Ref. [52], we investigate the contribution of the bulk states in terms of the electron density by using

$$R_{\text{bulk/surface}} = \frac{n_b d_{\text{TI}}}{n_s}, \quad (19)$$

where n_b is the bulk electron density of the TI with thickness d_{TI} and n_s is the surface electron density. We assume that the bulk state of a TI thin film is a quantum-well system along the z direction; namely, $E_{ks,\ell} = \hbar^2/(2m^*)\left(k_x^2 + k_y^2\right) + E_{z,\ell}(d_{\text{TI}}) + \Delta_c + s\Delta_b$, with $E_{z,\ell}(d_{\text{TI}}) = \hbar^2/(2m^*)\ell^2\pi^2/d^2$, where ℓ is an integer, m^* is the effective electron mass, and Δ_b is the exchange energy in the bulk of magnetic TIs with spin index $s = \pm$. The corresponding electron density is given by $n_b = \int_{-\infty}^{\infty} dE D_b(E) f(E)$ [$n_s = \int_{-\infty}^{\infty} dE D_s(E) f(E)$], where $D_b(E) = \sum_{ks} \delta(E - E_b)$ [$D_s(E) = \sum_{ks} \delta(E - E_s)$] is the bulk ($E_b = E_{ks,\ell}$) (surface [$E_s = E_{ks}$ in Eq. (2)]) density of states. The computed result is shown in Fig. 8(a). Consequently, we find that Eq. (19) is less than 10 % below 30 K for a Cr-doped BST thin film with $E_F = 95$ meV (corresponding carrier density approximately 10^{12} cm^{-2}), $\Delta_b = 30$ meV, and $m^*/m_0 = 0.15$ (m_0 is the free-electron mass) [73], which implies that the thermal excitation of the TI bulk states is negligible below 30 K.

For case (iii), we perform similar simulations including the random magnetic field at $T = 20$ K with an isotropic 3D Gaussian distribution [29]:

$$h_{th} = \sqrt{\frac{2k_B T \alpha_{eff}}{\mathcal{V} M_s \gamma \left(1 + \alpha_{eff}^2\right) \Delta t}}, \tag{20}$$

where $\mathcal{V} \approx l_x l_y d = 10^{-18}$ m^3 is the volume of the magnet, $\Delta t = 0.1$ ps, and parameters for Cr-doped BST are used. First, we investigate the effect of Eq. (20) on the pulsed-J_S-induced magnetization switching and find that the random magnetic field does not affect the switching diagram in Fig. 6 (a) up to 20 K. We also test the case of the pulsed-V_G-driven magnetization switching and show the result in Fig. 8 (b) for the extended input-parameter ranges. As seen, the influence of Eq. (20) emerges in the longer pulse region with larger V_S, reflecting randomness of the thermal fluctuation, whereas we confirm that stable magnetization switching is achieved in the wide parameter range. Note that the thermal stability of the magnet $K_u \mathcal{V}/k_B T \approx 5.2 \times 10^5$ at $E_F = 30$ meV ($V_G = 0$) and $T = 20$ K satisfies the required condition (greater than 60) for a nonvolatile memory.

V. SUMMARY

In summary, we present two distinct methods for magnetization switching by using electric field control of the SOT and MAE in TI–magnetic-TI hybrid systems. We formulate analytically the uniaxial magnetic anisotropy in magnetic TIs as a function of the Fermi level and show that the out-of-plane magnetization is always favored for the partially occupied surface band. We further propose a transistorlike device with the functionality of a nonvolatile magnetic memory adopting (i) the VCMA writing method that requires no external magnetic field and (ii) read out based on the anomalous Hall effect. For the magnetization reversal, by our using parameters of Cr-doped BST, the estimated source-drain current density and gate voltage are on the order of 10^4–10^5 A/cm^2 and 0.1 V, respectively, below 20 K. As a conclusion of this study, we show the switching phase diagram for the input pulse width and voltages as a guide for realizing the proposed magnetization-reversal method. We also discuss the possibility of magnetization switching by the proposed method in TI/FI bilayers with the magnetic proximity effect. Similar magnetization switching may be achieved by the FI layer with 2D van der Waals ferromagnetic semiconductors or rare-earth iron garnets near their compensation point. However, the compensation points of the FIs are at a finite temperature, so the thermal excitation of the TI bulk state and the effective magnetic field due to the thermal fluctuation of localized moments might affect the switching probability, which is beyond the scope of the present investigation. Simultaneous control of the magnetic anisotropy and SOT by an electric gate may lead to low-power memory and logic devices utilizing TIs.

APPENDIX A: CURRENT EXPRESSION FOR SOT

We rewrite the SOT in terms of a current density flowing on the magnetized TI surface. According to Eq. (6), the current-induced spin polarization involving $\mathbf{J}_S = \sigma_L \mathbf{E}/d = (\sigma_L/d)(V_S/l_x)\hat{\mathbf{x}}$ (in the unit of amperes per square meter) is given by

$$\boldsymbol{\mu} = -\frac{d}{ev_F} \left(-\theta_{AH}\mathbf{J}_S + \hat{\mathbf{z}} \times \mathbf{J}_S\right), \tag{A1}$$

where

$$\theta_{AH} \equiv \frac{\sigma_{AH}}{\sigma_L} = \frac{8\hbar}{E_F \tau} \frac{\Delta m_z E_F \left(E_F^2 + \Delta^2 m_z^2\right)}{\left(E_F^2 - \Delta^2 m_z^2\right)\left(E_F^2 + 3\Delta^2 m_z^2\right)} \tag{A2}$$

is an anomalous Hall angle. Inserting Eq. (A1) into Eq. (3), we obtain the current expression for the SOT:

$$\mathbf{T}_{SO} = \frac{\gamma \Delta}{ev_F M_s} \mathbf{m} \times \theta_{AH}\mathbf{J}_S - \frac{\gamma \Delta}{ev_F M_s} \mathbf{m} \times \left(\hat{\mathbf{z}} \times \mathbf{J}_S\right). \tag{A3}$$

Recalling that the first term is responsible for the DL torque associated with a magnetoelectric coupling, one may expect that a giant current-induced SOT is obtained by Eq. (A2) in the case of $E_F \approx \Delta m_z$. However, $\mathbf{J}_S$ then becomes nearly zero because the relation between θ_{AH} and $\mathbf{J}_S$ is a trade-off [see Eq. (5)], and therefore in Eq. (A2) one should not seek the reason for a giant current-induced SOT in recent experiments [6–8].

APPENDIX B: ELECTRIC FIELD EFFECT ON E_F

We model the electrical modulation of E_F by the gate voltage V_G of the device proposed in the main text (Fig. 3). According to Gauss's law, an induced charge accumulation per unit area (q_e) on the TI surface is described by

$$\frac{q_e}{\epsilon} = \frac{V_G}{d_D}, \tag{B1}$$

where $q_e = en_c$, with the modulated electron density $n_c = \left[E_F(V_G)^2 - E_F(0)^2\right]/4\pi\left(\hbar v_F\right)^2$ [74]. Defining the intrinsic electron density as $n_{int} = \left[E_F(0)^2 - \Delta^2\right]/4\pi(\hbar v_F)^2$

and inserting it into Eq. (B1), we finally obtain Eq. (16) describing the electric field effect on E_F.

———

[1] A. Hoffmann and S. D. Bader, Opportunities at the Frontiers of Spintronics, Phys. Rev. Appl. **4**, 047001 (2015).

[2] A. Manchon, J. Železný, I. M. Miron, T. Jungwirth, J. Sinova, A. Thiaville, K. Garello, and P. Gambardella, Current-induced spin-orbit torques in ferromagnetic and antiferromagnetic systems, Rev. Mod. Phys. **91**, 035004 (2019).

[3] L. Liu, O. J. Lee, T. J. Gudmundsen, D. C. Ralph, and R. A. Buhrman, Current-Induced Switching of Perpendicularly Magnetized Magnetic Layers Using Spin Torque from the Spin Hall Effec, Phys. Rev. Lett. **109**, 096602 (2012).

[4] J. Kim, J. Sinha, M. Hayashi, M. Yamanouchi, S. Fukami, T. Suzuki, S. Mitani, and H. Ohno, Layer thickness dependence of the current-induced effective field vector in Ta—CoFeB—MgO, Nat. Mater. **12**, 240 (2012).

[5] I. M. Miron, K. Garello, G. Gaudin, P. J. Zermatten, M. V. Costache, S. Auffret, S. Bandiera, B. Rodmacq, A. Schuhl, and P. Gambardella, Perpendicular switching of a single ferromagnetic layer induced by in-plane current injection, Nature (London) **476**, 189 (2011).

[6] Y. Fan, P. Upadhyaya, X. Kou, M. Lang, S. Takei, Z. Wang, J. Tang, L. He, L.-T. Chang, M. Montazeri, G. Yu, W. Jiang, T. Nie, R. N. Schwartz, Y. Tserkovnyak, and K. L. Wang, Magnetization switching through giant spin-orbit torque in a magnetically doped topological insulator heterostructure, Nat. Mater. **13**, 699 (2014).

[7] A. R. Mellnik, J. S. Lee, A. Richardella, J. L. Grab, P. J. Mintun, M. H. Fischer, A. Vaezi, A. Manchon, E.-A. Kim, N. Samarth, and D. C. Ralph, Spin-transfer torque generated by a topological insulator, Nature **511**, 449 (2014).

[8] Y. Wang, P. Deorani, K. Banerjee, N. Koirala, M. Brahlek, S. Oh, and H. Yang, Opological Surface States Originated Spin-Orbit Torques in Bi_2Se_3, Phys. Rev. Lett. **114**, 257202 (2015).

[9] D. Pesin and A. H. MacDonald, Spintronics and pseudospintronics in graphene and topological insulators, Nat. Mater. **11**, 409 (2012).

[10] Y. Ando, Topological insulator materials, J. Phys. Soc. Jpn. **82**, 102001 (2013).

[11] K. Kondou, R. Yoshimi, A. Tsukazaki, Y. Fukuma, J. Matsuno, K. S. Takahashi, M. Kawasaki, Y. Tokura, and Y. Otani, Fermi-level-dependent charge-to-spin current conversion by Dirac surface states of topological insulators, Nat. Phys. **12**, 1027 (2016).

[12] I. Garate and M. Franz, Inverse Spin-Galvanic Effect in the Interface between a Topological Insulator and a Ferromagnet, Phys. Rev. Lett. **104**, 146802 (2010).

[13] T. Yokoyama, Current-induced magnetization reversal on the surface of a topological insulator, Phys. Rev. B **84**, 113407 (2011).

[14] F. Mahfouzi, B. K. Nikolić, and N. Kioussis, Antidamping spin-orbit torque driven by spin-flip reflection mechanism on the surface of a topological insulator: A time-dependent nonequilibrium Green function approach, Phys. Rev. B **93**, 115419 (2016).

[15] P. B Ndiaye, C. A. Akosa, M. H. Fischer, A. Vaezi, E-A. Kim, and A. Manchon, Dirac spin-orbit torques and charge pumping at the surface of topological insulators, Phys. Rev. B **96**, 014408 (2017).

[16] Y. Fan, X. Kou, P. Upadhyaya, Q. Shao, L. Pan, M. Lang, X. Che, J. Tang, M. Montazeri, K. Murata, L.-T. Chang, M. Akyol, G. Yu, T. Nie, K. L. Wong, J. Liu, Y. Wang, Y. Tserkovnyak, and K. L. Wang, Electric-field control of spin-orbit torque in a magnetically doped topological insulator, Nat. Nanotechnol. **11**, 352 (2016).

[17] K. Yasuda, A. Tsukazaki, R. Yoshimi, K. Kondou, K. S. Takahashi, Y. Otani, M. Kawasaki, and Y. Tokura, Current-Nonlinear Hall Effect and Spin-Orbit Torque Magnetization Switching in a Magnetic Topological Insulator, Phys. Rev. Lett. **119**, 137204 (2017).

[18] J. Han, A. Richardella, S. A. Siddiqui, J. Finley, N. Samarth, and L. Liu, Room-Temperature Spin-Orbit Torque Switching Induced by a Topological Insulator, Phys. Rev. Lett. **119**, 077702 (2017).

[19] Y. Wang, D. Zhu, Y. Wu, Y. Yang, J. Yu, R. Ramaswamy, R. Mishra, S. Shi, M. Elyasi, K.-L. Teo, Y. Wu, and H. Yang, Room temperature magnetization switching in topological insulator-ferromagnet heterostructures by spin-orbit torques, Nat. Commun. **8**, 1364 (2017).

[20] M. Dc, R. Grassi, J.-Y. Chen, M. Jamali, D. Reifsnyder Hickey, D. Zhang, Z. Zhao, H. Li, P. Quarterman, Y. Lv, M. Li, A. Manchon, K. A. Mkhoyan, T. Low, and J.-P. Wang, Room-temperature high spin-orbit torque due to quantum confinement in sputtered $Bi_xSe_{(1-x)}$ films, Nat. Mater. **17**, 800 (2018).

[21] H. Wu, Y. Xu, P. Deng, Q. Pan, S. A. Razavi, K. Wong, L. Huang, B. Dai, Q. Shao, G. Yu, X. Han, J.-C. Rojas-Sanchez, S. Mangin, and K. L. Wang, Spin-orbit torque switching of a nearly compensated ferrimagnet by topological surface states, Adv. Mater. **31**, 1901681 (2019).

[22] H. Wu, P. Zhang, P. Deng, Q. Lan, Q. Pan, S. A. Razavi, X. Che, L. Huang, B. Dai, K. Wong, X. Han, and K. L. Wang, Room-Temperature Spin-Orbit Torque from Topological Surface States, Phys. Rev. Lett. **123**, 207205 (2019).

[23] P. Li *et al.*, Magnetization switching using topological surface states, Sci. Adv. **5**, eaaw3415 (2019).

[24] D. Chiba, M. Sawicki, Y. Nishitani, Y. Nakatani, F. Matsukura, and H. Ohno, Magnetization vector manipulation by electric fields, Nature **455**, 515 (2008).

[25] Y.-H. Chu, L. W. Martin, M. B. Holcomb, M. Gajek, S.-J. Han, Q. He, N. Balke, C.-H. Yang, D. Lee, W. Hu, Q. Zhan, P.-L. Yang, A. Fraile-Rodríguez, A. Scholl, S. X. Wang, and R. Ramesh, Electric-field control of local ferromagnetism using a magnetoelectric multiferroic, Nat. Mater. **7**, 478 (2008).

[26] M. Weisheit, S. Fähler, A. Marty, Y. Souche, C. Poinsignon, and D. Givord, Electric field-induced modification of magnetism in thin-film ferromagnets, Science **315**, 349 (2007).

[27] C.-G. Duan, J. P. Velev, R. F. Sabirianov, Z. Zhu, J. Chu, S. S. Jaswal, and E. Y. Tsymbal, Surface Magnetoelectric Effect in Ferromagnetic Metal Films, Phys. Rev. Lett. **101**, 137201 (2008).

[28] T. Maruyama, Y. Shiota, T. Nozaki, K. Ohta, N. Toda, M. Mizuguchi, A. A. Tulapurkar, T. Shinjo, M. Shiraishi, S.

Mizukami, Y. Ando, and Y. Suzuk, Large voltage-induced magnetic anisotropy change in a few atomic layers of iron, Nat. Nanotech. **4,** 158 (2009).

[29] Y. Shiota, T. Nozaki, F. Bonell, S. Murakami, T. Shinjo, and Y. Suzuki, Induction of coherent magnetization switching in a few atomic layers of FeCo using voltage pulses, Nat. Mater. **11,** 39 (2012).

[30] S.-H. C. Baek, K.-W. Park, D.-S. Kil, Y. Jang, J. Park, K.-J. Lee, and B.-G. Park, Complementary logic operation based on electric-field controlled spin-orbit torques, Nat. Electron. **1,** 398 (2018).

[31] R. Mishra, F. Mahfouzi, D. Kumar, K. Cai, M. Chen, X. Qiu, N. Kioussis, and H. Yang, Electric-field control of spin accumulation direction for spin-orbit torques, Nat. Commun. **10,** 248 (2019).

[32] J. Wang, B. Lian, and S.-C. Zhang, Electrically Tunable Magnetism in Magnetic Topological Insulators, Phys. Rev. Lett. **115,** 036805 (2015).

[33] A. Sekine and T. Chiba, Electric-field-induced spin resonance in antiferromagnetic insulators: Inverse process of the dynamical chiral magnetic effect, Phys. Rev. B **93,** 220403(R) (2016).

[34] Y. G. Semenov, X. Duan, and K. W. Kim, Electrically controlled magnetization in ferromagnet-topological insulator heterostructures, Phys. Rev. B **82,** 161406(R) (2012).

[35] M. E. Flatté, Voltage-driven magnetization control in topological insulator/magnetic insulator heterostructures, AIP Adv. **7,** 055923 (2017).

[36] Z. Jiang, C. Chang, C. Tang, P. Wei, J. S. Moodera, and J. Shi, Independent tuning of electronic properties and induced ferromagnetism in topological insulators with heterostructure approach, Nano Lett. **40,** 5835 (2015).

[37] T. Hirahara, S. V. Eremeev, T. Shirasawa, Y. Okuyama, T. Kubo, R. Nakanishi, R. Akiyama, A. Takayama, T. Hajiri, S. Ideta, *et al.*, Large-gap magnetic topological heterostructure formed by subsurface incorporation of a ferromagnetic layer, Nano Lett. **17,** 3493 (2017).

[38] Y. T. Fanchiang, K. H. M. Chen, C. C. Tseng, C. C. Chen, C. K. Cheng, S. R. Yang, C. N. Wu, S. F. Lee, M. Hong, and J. Kwo, Strongly exchange-coupled and surface-state-modulated magnetization dynamics in Bi_2Se_3/yttrium iron garnet heterostructures, Nat. Commun. **9,** 223 (2018).

[39] K. Nomura and N. Nagaosa, Electric charging of magnetic textures on the surface of a topological insulator, Phys. Rev. B **82,** 161401(R) (2010).

[40] T. Yokoyama, J. Zang, and N. Nagaosa, Theoretical study of the dynamics of magnetization on the topological surface, Phys. Rev. B **81,** 241410(R) (2010).

[41] A. Sakai and H. Kohno, Spin torques and charge transport on the surface of topological insulator, Phys. Rev. B **89,** 165307 (2014).

[42] T. Chiba, S. Takahashi, and G. E. W. Bauer, Magnetic-proximity-induced magnetoresistance on topological insulators, Phys. Rev. B **95,** 094428 (2017).

[43] S. Ghosh and A. Manchon, Spin-orbit torque in a three-dimensional topological insulator-ferromagnet heterostructure: Crossover between bulk and surface transport, Phys. Rev. B **97,** 134402 (2018).

[44] N. A. Sinitsyn, A. H. MacDonald, T. Jungwirth, V. K. Dugaev, and J. Sinova, Anomalous Hall effect in a

two-dimensional Dirac band: The link between the Kubo-Streda formula and the semiclassical Boltzmann equation approach, Phys. Rev. B **75,** 045315 (2007).

[45] D. Culcer and S. D. Sarma, Anomalous Hall response of topological insulators, Phys. Rev. B **83,** 245441 (2011).

[46] I. A. Ado, I. A. Dmitriev, P. M. Ostrovsky, and M. Titov, Anomalous Hall effect with massive Dirac fermions, Europhys. Lett. **111,** 37004 (2015).

[47] A. Sabzalipour, J. Abouie, and S. H. Abedinpour, Anisotropic conductivity in magnetic topological insulators, J. Phys.: Condens. Matter **27,** 115301 (2015).

[48] H. Li, H. Gao, L. P. Zârbo, K. Výborný, X. Wang, I. Garate, F. Doĝan, A. Ĉejchan, J. Sinova, T. Jungwirth, and A. Manchon, Intraband and interband spin-orbit torques in non-centrosymmetric ferromagnets, Phys. Rev. B **91,** 134402 (2015).

[49] K.-S. Lee, D. Go, A. Manchon, P. M. Haney, M. D. Stiles, H.-W. Lee, and K.-J. Lee, Angular dependence of spin-orbit spin-transfer torques, Phys. Rev. B **91,** 144401 (2015).

[50] Y. Tokura, K. Yasuda, and A. Tsukazaki, Magnetic topological insulators, Nat. Rev. Phys. **1,** 126 (2019).

[51] M. Mogi, T. Nakajima, V. Ukleev, A. Tsukazaki, R. Yoshimi, M. Kawamura, K. S. Takahashi, T. Hanashima, K. Kakurai, T. Arima, M. Kawasaki, and Y. Tokura, Large Anomalous Hall Effect in Topological Insulators with Proximitized Ferromagnetic Insulators, Phys. Rev. Lett. **123,** 016804 (2019).

[52] T. Chiba and S. Takahashi, Transport properties on an ionically disordered surface of topological insulators: Toward high-performance thermoelectrics, J. Appl. Phys. **126,** 245704 (2019).

[53] C.-Z. Chang, J. Zhang, X. Feng, J. Shen, Z. Zhang, M. Guo, K. Li, Y. Ou, P. Wei, *et al.*, Experimental observation of the quantum anomalous Hall effect in a magnetic topological insulator, Science **340,** 167 (2013).

[54] J. Ieda, S. E. Barnes, and S. Maekawa, Magnetic anisotropy by Rashba spin-orbit coupling in antiferromagnetic thin films, J. Phys. Soc. Jpn. **87,** 053703 (2018).

[55] Y. Tserkovnyak, D. A. Pesin, and D. Loss, Spin and orbital magnetic response on the surface of a topological insulator, Phys. Rev. B **91,** 041121(R) (2015).

[56] R. Yoshimi, K. Yasuda, A. Tsukazaki, K. S. Takahashi, N. Nagaosa, M. Kawasaki, and Y. Tokura, Quantum Hall states stabilized in semi-magnetic bilayers of topological insulators, Nat. Commun. **6,** 8530 (2015).

[57] C.-Z. Chang, J. Zhang, M. Liu, Z. Zhang, X. Feng, K. Li, L.-L. Wang, X. Chen, X. Dai, Z. Fang, X.-L. Qi, S.-C. Zhang, Y. Wang, K. He, X.-C. Ma, and Q.-K. Xue, Thin films of magnetically doped topological insulator with carrier-independent long-range ferromagnetic order, Adv. Mater. **25,** 1065 (2013).

[58] M. Jamali, J. S. Lee, J. S. Jeong, F. Mahfouzi, Y. Lv, Z. Zhao, B. K. Nikolić, K. A. Mkhoyan, N. Samarth, and J.-P. Wang, Giant spin pumping and inverse spin hall effect in the presence of surface and bulk spin-orbit coupling of topological insulator Bi_2Se_3, Nano Lett. **15,** 7126 (2015).

[59] A. Okada, S. Kanai, M. Yamanouchi, S. Ikeda, F. Matsukura, and H. Ohno, Electric-field effects on magnetic anisotropy and damping constant in Ta/CoFeB/MgO

investigated by ferromagnetic resonance, Appl. Phys. Lett. **105**, 052415 (2014).

[60] T. Fujita, M. B. A. Jalil, and S. G. Tan, Topological insulator cell for memory and magnetic sensor applications, Appl. Phys. Express **4**, 094201 (2011).

[61] K. Takiguchi, L. D. Anh, T. Chiba, T. Koyama, D. Chiba, and M. Tanaka, Giant gate-controlled proximity magnetoresistance in semiconductor-based ferromagnetic-non-magnetic bilayers, Nat. Phys. **15**, 1134 (2019).

[62] S. Khan, C. W. Zollitsch, D. M. Arroo, H. Cheng, I. Verzhbitskiy, A. Sud, Y. P. Feng, G. Eda, and H. Kurebayashi, Spin dynamics study in layered van der Waals single-crystal $Cr_2Ge_2Te_6$, Phys. Rev. B **100**, 134437 (2019).

[63] C. Tang, P. Sellappan, Y. Liu, Y. Xu, J. E. Garay, and J. Shi, Anomalous Hall hysteresis in $Tm_3Fe_5O_{12}/Pt$ with strain-induced perpendicular magnetic anisotropy, Phys. Rev. B **94**, 140403(R) (2016).

[64] S. R. Yang, Y. T. Fanchiang, C. C. Chen, C. C. Tseng, Y. C. Liu, M. X. Guo, M. Hong, S. F. Lee, and J. Kwo, Evidence for exchange Dirac gap in magnetotransport of topological insulator-magnetic insulator heterostructures, Phys. Rev. B **100**, 045138 (2019).

[65] A. O. Leon, A. B. Cahaya, and G. E. W. Bauer, Voltage Control of Rare-Earth Magnetic Moments at the Magnetic-Insulator-Metal Interface, Phys. Rev. Lett. **120**, 027201 (2018).

[66] X.-L. Li, X. Duan, Y. G. Semenov, and K. W. Kim, Electrical switching of antiferromagnets via strongly spin-orbit coupled materials, J. Appl. Phys. **121**, 023907 (2017).

[67] T. Liu, J. Kally, T. Pillsbury, C. Liu, H. Chang, J. Ding, Y. Cheng, M. Hilse, R. E.-Herbert, A. Richardella, N. Samarth, and M. Wu, Changes of Magnetism in a Magnetic Insulator due to Proximity to a Topological Insulator, Phys. Rev. Lett. **125**, 017204 (2020).

[68] M. H. Fischer, A. Vaezi, A. Manchon, and E.-A. Kim, Spin-torque generation in topological insulator based heterostructures, Phys. Rev. B **93**, 125303 (2016).

[69] J. Zhang, J.-P. Velev, X. Dang, and E. Y. Tsymbal, Band structure and spin texture of Bi_2Se_3 3D ferromagnetic metal interface, Phys. Rev. B **94**, 014435 (2016).

[70] J. M. Marmolejo-Tejada, K. Dolui, P. Lazić, P.-H. Chang, S. Smidstrup, D. Stradi, K. Stokbro, and B. K. Nikolić, Proximity band structure and spin textures on both sides of topological-insulator/Ferromagnetic-Metal interface and their charge transport probes, Nano Lett. **17**, 5626 (2017).

[71] J.-Y. Li, R.-Q. Wang, M.-X. Deng, and M. Yang, In-plane magnetization effect on current-induced spin-orbit torque in a ferromagnet/topological insulator bilayer with hexagonal warping, Phys. Rev. B **99**, 155139 (2019).

[72] T. Arakane, T. Sato, S. Souma, K. Kosaka, K. Nakayama, M. Komatsu, T. Takahashi, Z. Ren, K. Segawa, and Y. Ando, Tunable Dirac cone in the topological insulator $Bi_{2-x}Sb_xTe_{3-y}Se_y$, Nat. Commun. **3**, 636 (2012).

[73] N. P. Butch, K. Kirshenbaum, P. Syers, A. B. Sushkov, G. S. Jenkins, H. D. Drew, and J. Paglione, Strong surface scattering in ultrahigh-mobility Bi_2Se_3 topological insulator crystals, Phys. Rev. B **81**, 241301(R) (2010).

[74] T. Chiba, S. Takahashi, and T. Komine, Ambipolar Seebeck power generator based on topological insulator surfaces, Appl. Phys. Lett. **115**, 083107 (2019).